

28 **1. Introduction**

29 Terrestrial ecosystem evapotranspiration (E) is the primary pathway by which land surface
30 moisture returns to the atmosphere and thus plays a central role in the global water cycle (Liu et al.,
31 2023; Sun et al., 2022). E comprises three components: soil evaporation (Es), vegetation canopy
32 interception (Ei), and plant transpiration (T) (Niu et al., 2020; Wei et al., 2017). Among these,
33 vegetation transpiration, by which water is released to the atmosphere through plant stomata,
34 accounts for over 60% of total terrestrial E (Li et al., 2024; Wei et al., 2017). As transpiration is
35 closely linked to carbon assimilation and energy exchange, the vegetation transpiration fraction (TF,
36 defined as T/E) quantifies the contribution of vegetation to land–atmosphere water–vapor flux and
37 is a key indicator of vegetation–climate coupling strength (Schlesinger and Jasechko, 2014; Wei et
38 al., 2017). Understanding changes in TF is crucial for revealing ecohydrological mechanisms and
39 accurately predicting climate–change impacts.

40 Persistent climate warming and rising atmospheric CO₂ over the past few decades have driven
41 global vegetation greening and altered ecosystem water balances (Denissen et al., 2022; Hu et al.,
42 2023). Increases in Leaf area index (LAI) directly enhance canopy interception and transpiration
43 potential; global plant transpiration is estimated to have increased by about 6% from 1990–2020,
44 primarily as a consequence of increased LAI (Chen et al., 2024). However, the positive effect of
45 LAI on transpiration depends on water availability: when soil moisture (SM) is scarce or
46 atmospheric drought, often represented by vapor pressure deficit (VPD), intensifies, plants close
47 their stomata to suppress water loss, thereby reducing both transpiration and photosynthesis (Liu et
48 al., 2020; Zahra et al., 2023). SM represents the supply-side constraint, whereas VPD represents the
49 atmospheric demand-side pull; these two factors often co-vary and can together impose compound
50 drought stress on ecosystems (Song et al., 2024). High VPD induces partial stomatal closure to
51 prevent excessive water loss and hydraulic failure, causing transpiration rates per unit leaf area to
52 saturate or even decline under very high VPD conditions (Grossiord et al., 2020; Novick et al., 2016).
53 Therefore, even as LAI increases, the additional leaf area struggles to further increase T under
54 extreme atmospheric drought (Xu et al., 2023). Conversely, under moderate SM and appreciable
55 atmospheric demand, vegetation can maintain both water supply and evaporative demand at levels
56 that support transpiration, allowing increases in LAI to exert a stronger positive effect on TF (Liu

57 et al., 2020). During extreme soil drought, increased surface sensible heat further dries the near-
58 surface atmosphere, creating positive SM–VPD feedback that exacerbates drought conditions (Qing
59 et al., 2022; Zhou et al., 2019). Accurately characterizing the response of TF to changes in LAI
60 therefore requires a unified framework that accounts for the synergistic and nonlinear effects of both
61 soil water supply and atmospheric demand (Koehler et al., 2023). In recent years, discrepancies
62 have emerged regarding the relative roles of SM and VPD: some studies have emphasized that
63 atmospheric drought imposes greater limits on ecosystem water–carbon cycles (Novick et al., 2016),
64 whereas others, after decoupling the coupled effects of VPD and SM, have found that soil moisture
65 is the dominant factor, especially in semi-arid regions, where SM typically imposes a stronger
66 limitation on productivity (Liu et al., 2020). Because SM and VPD are often strongly correlated,
67 quantifying their relative roles under coupled hydroclimatic conditions remains a central challenge
68 in ecohydrological research.

69 Since the 1970s, China has implemented some of the world’s largest-scale afforestation and
70 ecological restoration programs, increasing forest cover from approximately 12% in the 1970s to
71 over 22% in recent years (Cheng et al., 2025). China’s forests now comprise extensive natural and
72 planted forests. Natural forests are concentrated mainly in the mountainous regions of northeastern
73 and southwestern China, whereas planted forests are more widespread in eastern, central, and
74 southern China (Cheng et al., 2024b). Compared with natural forests, planted forests in China are
75 more often younger, structurally simpler, and dominated by single-species or even-aged stands
76 under more intensive management (Cheng et al., 2024a; Farooq et al., 2021). These differences in
77 origin, structure, and water-use strategies may underlie substantial disparities between NF and PF
78 in soil water acquisition, stomatal regulation, and hydraulic safety margins, thereby leading to
79 different responses of TF to changes in LAI (hereafter, LAI–TF sensitivity, denoted as θ). Exploring
80 these disparities between forest types can deepen the understanding of vegetation water-use
81 mechanisms and improve regional water-resource management, afforestation benefit assessment,
82 and climate-adaptive forestry strategies. However, systematic research on this issue is currently
83 lacking. Existing studies have mostly examined the sensitivity of transpiration or productivity to
84 drought stress at global or broad regional scales (Liu et al., 2020; Novick et al., 2016) , or have
85 focused on ecohydrological processes in specific arid regions, without a comparative assessment of

86 θ across forest types along a unified climatic gradient. This raises four interrelated questions: (1)
87 Are there systematic differences in θ between NF and PF along the climatic gradient from humid to
88 semi-arid conditions? (2) How have these differences changed over the last 30 years? (3) Under
89 coupled changes in SM and VPD, what are the relative roles of these two factors in shaping θ , and
90 do these roles vary across climatic backgrounds or over time? (4) Through which hydrological
91 pathways (SM and/or VPD) do changes in macroclimate, such as radiation, precipitation,
92 temperature, and wind speed, indirectly affect θ ? Addressing these questions will help fill important
93 research gaps and deepen our understanding of forest–water relations under climate change.

94 The objectives of this study were to quantify the spatiotemporal patterns of transpiration
95 sensitivity (θ) in China’s natural forests (NF) and plantation forests (PF) from 1990 to 2020 and to
96 identify the hydroclimatic controls underlying these patterns. To this end, we integrated multi-
97 source remote-sensing and reanalysis data to derive growing-season LAI, evapotranspiration
98 components, and meteorological variables for forest pixels at 0.1° resolution. We first used the
99 aridity index (AI) framework to characterize the climatic background across four climatic zones and
100 then focused the statistical analyses on the humid, semi-humid, and semi-arid zones to ensure
101 comparability. We then applied complementary analytical approaches at different statistical scales:
102 pooled spatial binning was used to characterize the response surface of θ along the joint SM–VPD
103 gradient and to compare spatial contrasts under comparable hydroclimatic backgrounds, whereas
104 sliding-window partial correlation and ridge regression were used to quantify the independent
105 temporal associations of SM and VPD with θ and their evolution over time. Finally, pathway
106 analysis was used to decompose the indirect effects of macroclimate change on θ through local
107 hydrological pathways. All trends were estimated using the Theil–Sen slope and evaluated with the
108 Mann–Kendall test. We further assessed robustness through cross-product comparison and
109 examined whether atmospheric CO₂ and stand age altered the main interpretation. Together, this
110 framework was designed to reveal both the spatial heterogeneity and temporal evolution of
111 hydroclimatic controls on θ in China’s contrasting forest types.

112 **2. Materials and methods**

113 **2.1. Data**

114 We used datasets describing forest type, canopy structure, evapotranspiration components,

115 hydroclimate, and several auxiliary background factors (Table 1). Forest type data were obtained
116 from the 1990–2020 spatial distribution dataset of natural and plantation forests in China (Cheng et
117 al., 2024b). This dataset was derived from Landsat imagery and extensive forest inventory samples
118 using machine-learning classification and was resampled to 0.1° resolution to match the
119 hydroclimatic datasets. Pixels with 100% coverage of either natural forest (NF) or plantation forest
120 (PF) were treated as pure pixels, and only these pixels were included in all major analyses. To
121 maintain temporal consistency between forest masks and climate data, we adopted a period-based
122 dynamic matching strategy. Specifically, forest maps for 1990, 1995, 2000, 2005, 2010, 2015, and
123 2020 were used to represent the periods 1990–1994, 1995–1999, 2000–2004, 2005–2009, 2010–
124 2014, 2015–2019, and 2020, respectively.

125 LAI was derived from the GIMMS LAI4g dataset (Cao et al., 2023). The main
126 evapotranspiration dataset used in this study was GLEAM v4.2a, from which transpiration (T),
127 evapotranspiration (E), and soil moisture (SM) were extracted. GLEAM separately estimates the
128 major components of terrestrial evaporation and provides both surface and root-zone soil moisture.
129 In this study, SM refers to the root-zone soil moisture product, rather than surface soil moisture,
130 because it more closely represents plant-available water relevant to transpiration regulation at the
131 seasonal to interannual scales considered here. In GLEAM, root-zone soil moisture is represented
132 as a vegetation-accessible multi-layer soil profile constrained by assimilated surface observations,
133 rather than as a single shallow soil layer. Near-surface meteorological variables, including air
134 pressure (Pa), relative humidity (RH), air temperature (Ta), precipitation (P), dewpoint temperature
135 (Td), wind speed (WS), net radiation (Rn), and potential evapotranspiration (PET), were obtained
136 from ERA5-Land. All environmental variables were aggregated over the growing season (April–
137 October) for 1990–2020, using only growing-season data and excluding non-growing-season
138 observations. Means were used for state variables (e.g., LAI, SM, Ta, and VPD), whereas
139 cumulative values were used for flux variables (e.g., E, T, and P).

140 To evaluate the robustness of the estimated θ patterns and trends to data-product choice, we
141 additionally used two alternative gridded products for cross-product comparison in supplementary
142 analyses. One was the Simple Terrestrial Hydrosphere v2 (SiTHv2) product, which provides
143 independent estimates of evapotranspiration and transpiration (Zhang et al., 2024). The other was

144 the China terrestrial ecosystem transpiration fraction dataset (Niu et al., 2020), from which an
 145 alternative transpiration-fraction-based θ estimate was derived for comparison. These two datasets
 146 were used only for robustness assessment of θ , whereas all main calculations in the study were based
 147 on GLEAM.

148 To assess whether long-term changes in θ may also be modulated by non-hydroclimatic
 149 background factors, we further compiled several auxiliary datasets for supplementary analyses,
 150 including a global 1-km atmospheric carbon dioxide concentration dataset (Wang, 2025), a long-
 151 term reconstructed forest age dataset for China (Xia et al., 2024), and a 2020 forest age spatial
 152 distribution dataset for China (Cheng and Guo, 2024). These auxiliary datasets were resampled to
 153 0.1° resolution and used only to assess whether CO_2 and stand age materially altered the observed
 154 θ patterns and trends. They were not included in the main analytical framework, in which the focus
 155 was on hydroclimatic controls.

156 **Table 1. Data overview**

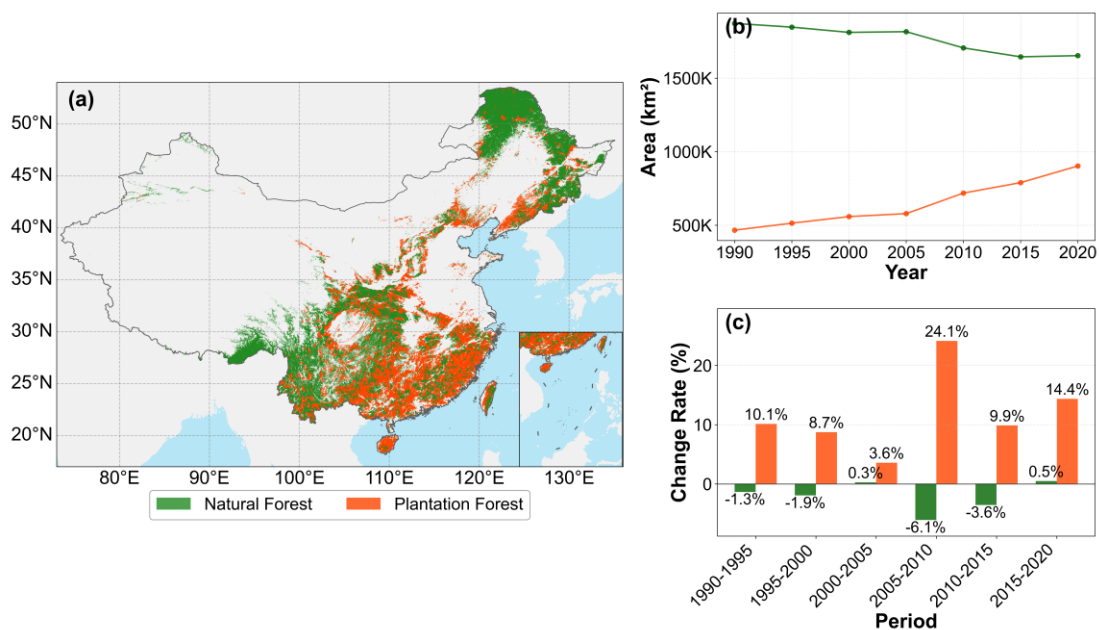
Variable	Data set	Resolution (spatial)	Resolution (temporal)	Time span	References
Forest type	Planted and natural forest maps in China from 1990 to 2020	1 km	5 years	1990– 2020	Cheng et al., 2024b
LAI	GIMMS LAI4g	$1/12^\circ$	15 day	1982– 2020	Cao et al., 2023
E, T, SM	GLEAM v4.2a	0.1°	1 day	1980– 2023	Miralles et al., 2025
Validation data	SiTHv2	0.1°	1 day	1982– 2020	Zhang et al., 2024
	China terrestrial ecosystem transpiration fraction dataset	0.05°	8 day	1981– 2015	Niu et al., 2020
Ta, Pa, RH, Td, P, PET, Rn, WS	ERA5-Land	0.1°	1 month	1950– 2025	Muñoz-Sabater et al., 2021
CO ₂	Global 1 km atmospheric carbon dioxide concentration dataset	1 km	annually	2003– 2023	Wang, 2025
forest age	Long-term reconstructed forest age dataset for China	1 km	annually	1980– 2015	Xia et al., 2024
	2020 forest age spatial distribution dataset for China	30 m	static	2020	Cheng et al., 2024a

157 LAI, Leaf area index; E, Evapotranspiration; T, Transpiration; SM, Root-zone soil moisture; Ta,

158 Air temperature; Td, Dewpoint temperature; Pa, Air pressure; P, Precipitation; PET, Potential
 159 evapotranspiration; Rn, Net radiation; WS, wind speed.

160 2.2. Study region

161 Our study area covers terrestrial China, spanning temperate, subtropical, and tropical climate
 162 zones. The analysis focuses on China's NF and PF. NF are mainly concentrated in the mountains of
 163 Northeast and Southwest China, whereas PF are widely distributed across the plains and hills of
 164 East, Central, and South China (Figure 1a). The vast majority of NF and PF are located in humid
 165 and semi-humid zones (Figure 2).

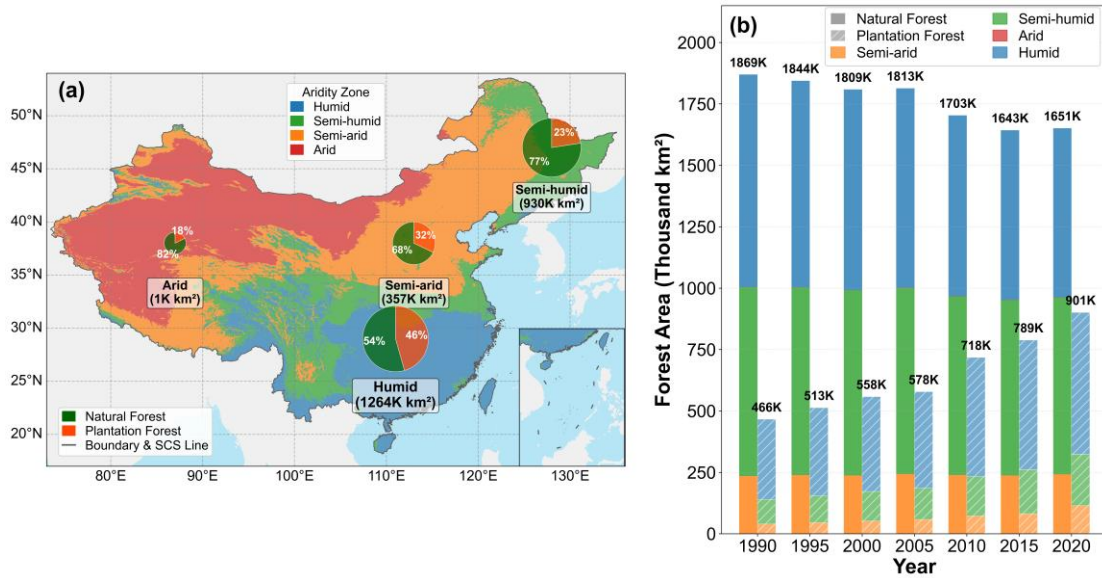


166
 167 **Figure 1. Spatiotemporal characteristics of China's natural forests (NF) and plantation forests**
 168 **(PF) from 1990 to 2020.** (a) Average spatial distribution of NF (green) and PF (orange) in China
 169 from 1990 to 2020. (b) Dynamic changes in the area (km²) of NF and PF from 1990 to 2020. (c)
 170 Rate of change (%) in NF and PF area for each five-year period from 1990–2020.

171 2.2.1. Aridity index and analytical framework

172 We used the aridity index (AI) to characterize climatic background and to organize the spatial
 173 analyses within a unified framework. AI was defined as the ratio of annual potential
 174 evapotranspiration to annual precipitation, $AI = PET / P$. Based on the 1990–2020 multi-year
 175 mean AI, China was divided into four climatic zones: humid ($AI < 1$), semi-humid ($1 \leq AI < 1.5$),
 176 semi-arid ($1.5 \leq AI < 4$), and arid ($AI \geq 4$) (Zhu et al., 2022). This four-zone classification was

177 used as the geographic framework for mapping and descriptive comparisons. Because forest
 178 samples in the arid zone were extremely sparse, subsequent statistical analyses were restricted to
 179 the humid, semi-humid, and semi-arid zones.



180
 181 **Figure 2. Spatiotemporal distribution and composition of forests in different climatic zones in**
 182 **China from 1990 to 2020.** (a) Spatial distribution of the four climatic zones (humid, semi-humid,
 183 semi-arid, and arid) in China; the pie charts show the total forest area within each zone and its
 184 composition of natural forest (green) and planted forest (orange). (b) Dynamic changes in forest
 185 area in each climatic zone from 1990 to 2020. For each year, the left solid stacked bar represents
 186 natural forest (NF), and the right hatched stacked bar represents plantation forest (PF). Bar colors
 187 indicate the forest area contributed by different climatic zones. The value at the top of each year
 188 indicates the total national forest area, and labels with “K” denote 10^3 km².

189 2.3. Methods

190 2.3.1. VPD calculation

191 Vapor pressure deficit (VPD, hPa) is expressed, as follows, as the difference between
 192 saturation vapor pressure (P_s , hPa) and actual vapor pressure (P_w , hPa):

$$193 \quad VPD = P_s - P_w \quad (1)$$

194 To calculate VPD, we used directly observed meteorological parameters, including air
 195 temperature (T_a , °C), relative humidity (RH , %), and air pressure (P_a , hPa). P_s was calculated using
 196 the improved Magnus equation (Yuan et al., 2019):

197
$$P_s = 6.112 \times f \times e^{\frac{17.67 \times T_a}{T_a + 243.5}} \quad (2)$$

198 Here, f is the atmospheric pressure enhancement factor, which corrects for the effect of pressure
 199 on saturation vapor pressure in moist air (Buck, 1981). This coefficient is calculated using P_a as
 200 follows:

201
$$f = 1 + 7 \times 10^{-4} + 3.46 \times 10^{-6} \times P_a \quad (3)$$

202 P_w is then derived from P_s and RH as follows :

203
$$P_w = P_s \times RH \times \frac{1}{100\%} \quad (4)$$

204 2.3.2. Sensitivity of TF to LAI

205 We define the transpiration fraction as

206
$$TF = \frac{T}{E} \quad (5)$$

207 In this study, T and E were first aggregated from daily data to annual growing-season totals
 208 (April–October), and LAI was represented by the corresponding annual growing-season mean. TF
 209 was then calculated from these annual growing-season quantities, and all subsequent θ analyses
 210 were therefore conducted at the annual growing-season scale rather than at the daily or monthly
 211 scale.

212 Note that $TF \in (0,1)$ is bounded. To explicitly account for the inherent nonlinearity and
 213 saturation in the TF–LAI relationship, we estimated the sensitivity θ as a marginal response under
 214 a bounded nonlinear framework.

215 Within the full period (1990–2020) and within each 11-year moving window, we fit a quadratic
 216 model in logit space:

217
$$z = \text{logit}(TF) = \ln\left(\frac{TF}{1-TF}\right) = a + b(LAI - LAI_{med}) + c(LAI - LAI_{med})^2 \quad (6)$$

218 Here, LAI_{med} is the pixel-specific median LAI within the same period (median-centering was used
 219 to improve numerical stability). Prior to the logit transform, TF was clipped to $[\varepsilon, 1 - \varepsilon]$ ($\varepsilon = 0.005$)
 220 to avoid numerical singularities.

221 We then recovered $TF = 1 / (1 + e^{-z})$ and computed the marginal sensitivity as

222
$$\theta = \frac{\partial TF}{\partial LAI} = TF(1-TF)[b + 2c(LAI - LAI_{med})] \quad (7)$$

223 For ease of interpretation, Eq. (7) can be written as

224
$$\theta = \underbrace{TF(1-TF)}_{damping} \times \underbrace{[b + 2c(LAI - LAI_{med})]}_{\eta}$$
, in which the damping term reflects boundary effects

225 and η represents the structural sensitivity in logit space.

226 To separate the position-dependent saturation effect from changes in the shape of the fitted TF-

227 LAI relationship, we evaluated (i) θ_{total} at $LAI = LAI_{med}$, representing the sensitivity under the

228 actual state of each pixel and (ii) θ_{clim} at a fixed reference LAI_{ref} (global median LAI), which

229 removes the influence of shifting along the TF-LAI curve. Additionally, the boundary component

230 was quantified as

231
$$\theta_{bound} = \theta_{total} - \theta_{clim} \quad (8)$$

232 We calculated θ at two time scales. (1) The full-period mean θ characterized the average state

233 during 1990–2020. (2) The θ time series characterized decadal changes, generated using an 11-year

234 moving window recorded for the central year (1995–2015), a data processing step that was also used

235 for subsequent trend and attribution analyses. Pixels with insufficient valid years and negligible LAI

236 variability were excluded to ensure robustness.

237 **2.3.3. Spatial association under the joint SM–VPD gradient: binning analysis**

238 To assess the relative roles of SM and VPD in the spatial differentiation of θ , we applied a

239 pooled spatial-binning analysis. Using all eligible pure NF and pure PF pixels as samples, we

240 extracted the full-period mean θ , SM, and VPD values and Z-score standardized them. To evaluate

241 the relative effect of VPD under comparable SM backgrounds, denoted as $\Delta\theta(\text{VPD}|\text{SM})$, pixels

242 were first grouped into bins according to SM. Within each SM bin, the difference in mean θ between

243 high- and low-VPD groups was calculated, and these differences were then averaged across bins.

244 The relative effect of SM, denoted as $\Delta\theta(\text{SM}|\text{VPD})$, was evaluated in the same way by binning

245 pixels according to VPD and then comparing high- and low-SM groups within each bin. This

246 approach thus summarized spatial contrasts under comparable hydroclimatic backgrounds using a

247 control-variable logic. These analyses are complementary but not identical to the subsequent

248 temporal attribution analyses; specifically, the binning analysis characterized cross-site contrasts in

249 θ across the long-term SM–VPD climate space, whereas the partial-correlation and ridge analyses

250 quantified within-pixel temporal associations of θ with SM and VPD.

251 **2.3.4. Dynamic temporal attribution: partial correlation and ridge regression**

252 To investigate the pixel-scale temporal relationships of SM and VPD with θ , we used partial
253 correlation and ridge regression based on the 1995–2015 11-year sliding-window series. This
254 analysis was conducted at two levels. First, for each pixel, we calculated an overall partial
255 correlation coefficient and ridge-regression coefficient based on the full 1995–2015 series,
256 representing the average independent association of SM and VPD with θ throughout that period
257 after accounting for their covariation. Second, to evaluate change over time, we performed a
258 secondary sliding-window analysis on the same 1995–2015 series and generated time series of the
259 coefficients themselves. Trends in these coefficient series were then used to infer whether the effects
260 of SM and VPD became stronger or weaker over time. Thus, the first-level analysis described the
261 mean temporal attribution pattern, whereas the second-level analysis characterized its change over
262 time.

263 Partial correlation analysis: We calculated two pixel-wise partial correlation coefficients: $r(\theta,$
264 $SM|VPD)$ and $r(\theta, VPD|SM)$. The former represents the correlation between θ and SM after
265 controlling for interannual VPD fluctuations, whereas the latter represents the correlation between
266 θ and VPD after controlling for SM variability.

267 Ridge regression analysis: Given the collinearity between SM and VPD, we further employed
268 a ridge regression model, $\theta = \beta_{SM} \cdot SM + \beta_{VPD} \cdot VPD$, to more robustly quantify their relative
269 contributions to θ . By introducing an L2 regularization term, ridge regression stabilizes coefficient
270 estimates under multicollinearity. The regression was performed on standardized time series, and
271 the resulting coefficients (β_{SM} and β_{VPD}) directly reflect the relative strengths of the SM and VPD
272 effects. We further calculated the relative contribution (RC) of SM and VPD as
273 $RC_{SM} = |\beta_{SM}| / (|\beta_{SM}| + |\beta_{VPD}|)$ and $RC_{VPD} = |\beta_{VPD}| / (|\beta_{SM}| + |\beta_{VPD}|)$, to determine the
274 dominant hydrological driver at each pixel. To further diagnose multicollinearity between SM and
275 VPD, we also calculated the variance inflation factor (VIF).

276 To quantify temporal changes in θ and in the coefficient series derived from the 11-year
277 moving-window analysis, we estimated trends using the Theil–Sen median slope estimator. Trend

278 significance was assessed using the Mann–Kendall (MK) test (two-tailed, $\alpha = 0.05$). To reduce
279 potential bias caused by temporal autocorrelation, the MK statistic was variance-corrected. The
280 same trend-analysis framework was applied consistently to all moving-window-derived time series
281 used in the temporal attribution analysis.

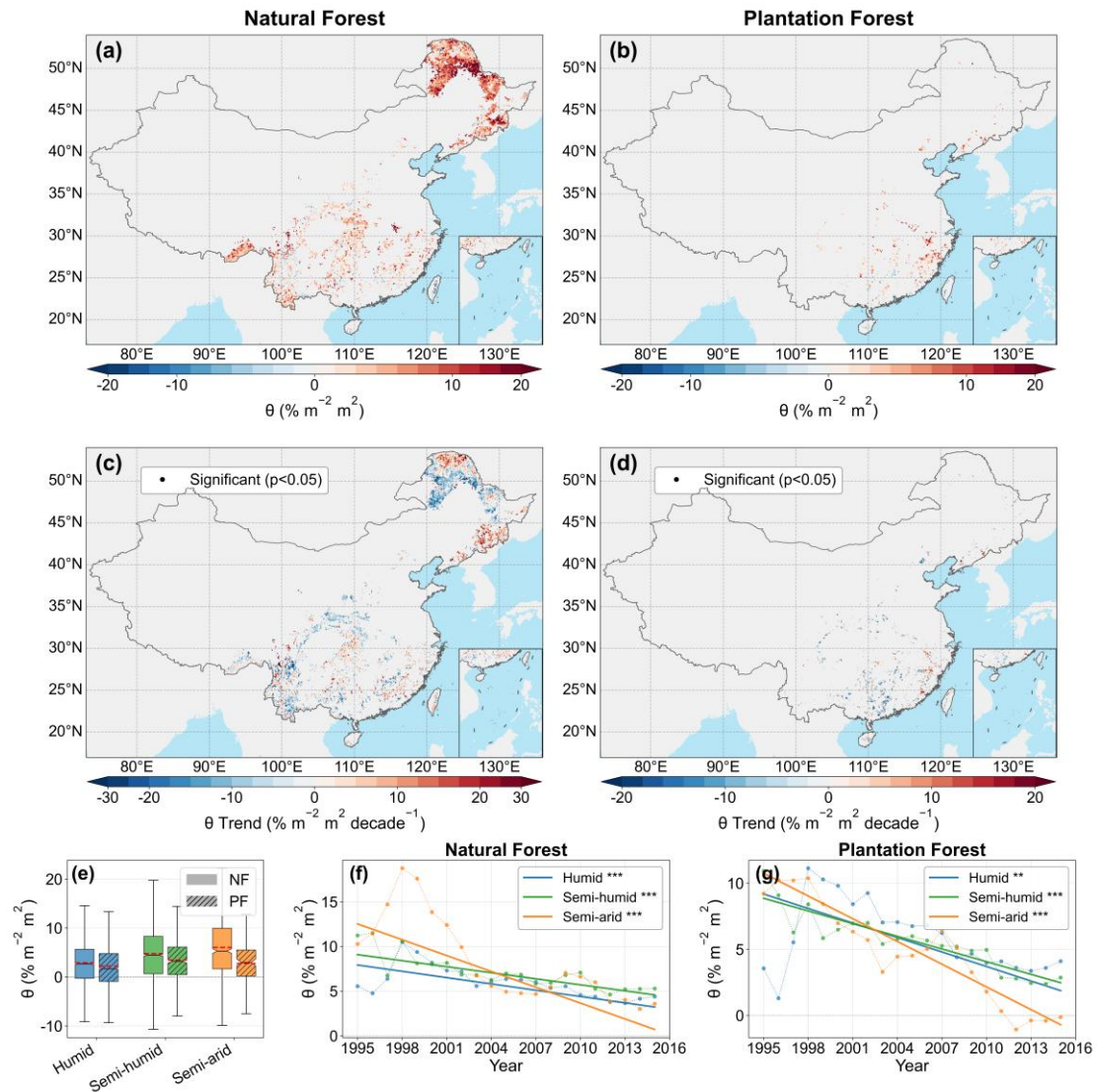
282 **2.3.5. Pathway analysis of macroclimate effects on θ**

283 To analyze the pathways through which macroclimate change may affect θ via local
284 hydrological processes, we constructed a pathway model. The independent variable X served as the
285 climate-factor trend (including P, Ta, Rn, and WS), the mediator variable M corresponded to the
286 local water supply–demand status (SM and VPD trends), and the dependent variable Y represented
287 the θ trend. RH was not included separately because its effect on atmospheric water demand is
288 already represented by VPD. Pathway analysis was used to partition the associations between
289 macroclimate trends and θ into direct effects and indirect effects mediated through SM and VPD.
290 The statistical significance of all pathway effects was tested by bootstrap resampling (1000
291 iterations). Because SM and VPD may remain correlated under coupled hydroclimatic conditions,
292 the pathway coefficients were interpreted as complementary association pathways rather than as a
293 strict causal separation of two fully independent mediators. This interpretation was further evaluated
294 using a supplementary mediator-specification comparison based on SM-only, VPD-only, and joint
295 pathway models (Figure S19). The trends of P, Ta, Rn, WS, SM, VPD, and θ used in the pathway
296 analysis were all estimated using the same Theil–Sen and variance-corrected Mann–Kendall
297 framework described above.

298
299

3. Results

3.1. Spatiotemporal patterns and long-term trends of θ



300

301 **Figure 3. Spatiotemporal patterns and long-term trends of LAI—TF sensitivity (θ) in China's**

302 **natural forests (NF) and plantation forests (PF) during the 1990–2020 growing seasons. (a)**

303 **and (b) show the multi-year mean spatial distribution of θ for NF and PF, respectively, derived from**

304 **the overall logit–quadratic model using TF_E (c) and (d) show the corresponding long-term trends in**

305 **θ estimated from the 11-year moving-window time series using the Theil–Sen slope; black dots**

306 **indicate significant trends based on the Mann–Kendall test ($p < 0.05$).** (e) shows the distribution

307 of θ across climatic zones (humid, semi-humid, and semi-arid) for NF and PF. (f) and (g) show the

308 temporal evolution of zone-averaged θ for NF and PF, respectively, with Theil–Sen trend lines

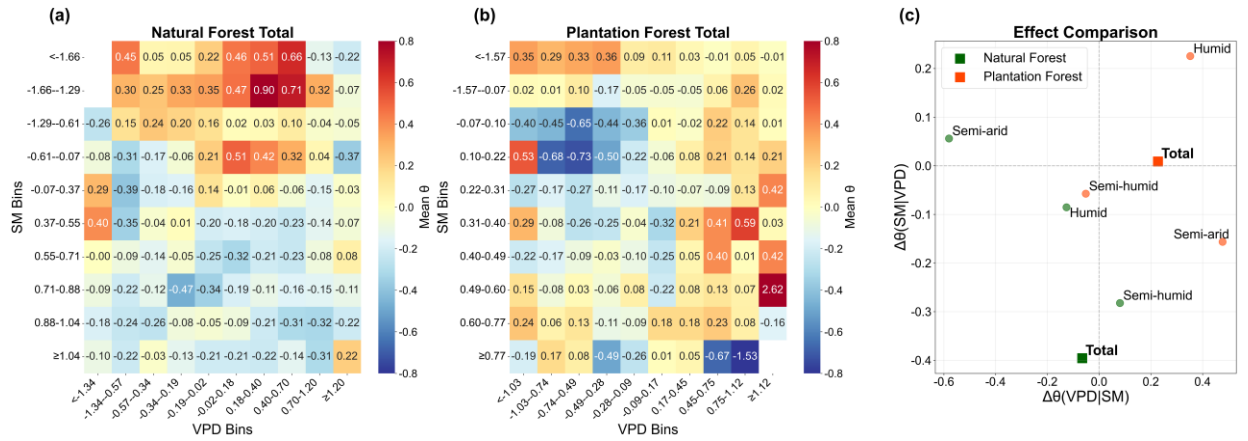
309 overlaid.

310 Mean θ showed clear spatial heterogeneity and was consistently higher in NF than in PF

311 (Figure 3a, b, e). High- θ areas in NF were concentrated mainly within the semi-arid to semi-humid
 312 transition belt, whereas PF showed a distinctly more fragmented pattern. During 1990–2020,
 313 growing-season θ declined widely in both forest types, with a stronger mean decline in PF than in
 314 NF (Figure 3c, d). Significant negative trends were concentrated mainly in semi-humid and semi-
 315 arid transition regions, while humid regions showed weaker negative trends. The zone-averaged
 316 time series further confirmed that θ decreased significantly across climatic zones in both forest types,
 317 with the strongest declines occurring under drier climatic conditions (Figure 3f, g). Overall, the
 318 marginal enhancement of TF by increasing LAI weakened over the past three decades, especially in
 319 PF and in relatively dry regions.

320 3.2. Hydroclimatic controls of θ : SM and VPD

321 3.2.1. Response of θ to the joint SM–VPD gradient



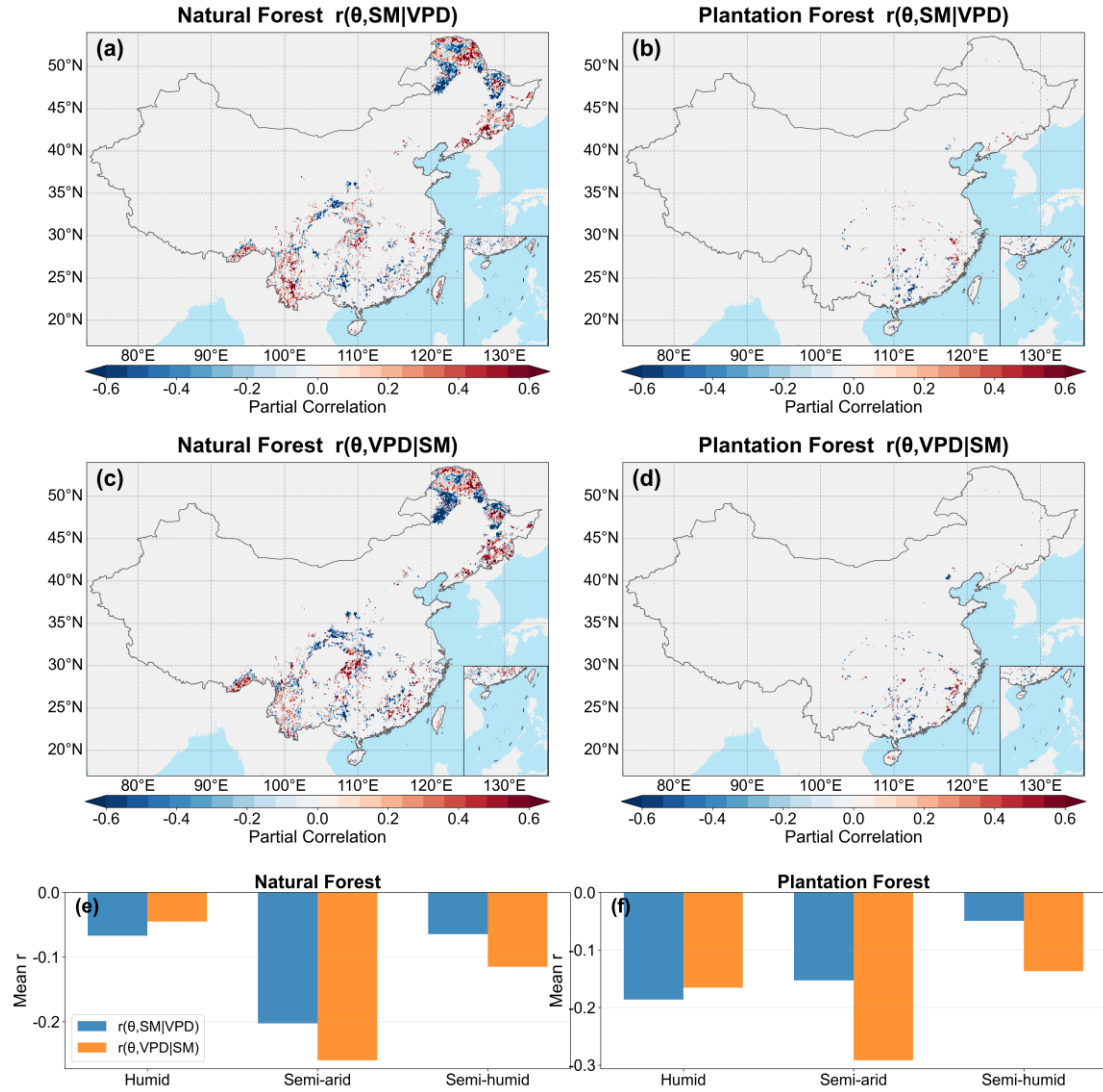
322 **Figure 4. Pooled spatial binning analysis of LAI–TF sensitivity (θ) under the joint soil**
 323 **moisture (SM)–vapor pressure deficit (VPD) gradient during the 1990–2020 growing seasons.**
 324 (a) and (b) show the mean standardized θ values in 10×10 SM–VPD bins for natural forests (NF)
 325 and plantation forests (PF), respectively; only bins with sample size ≥ 10 are shown. (c) shows
 326 the relative effects of VPD and SM as indicated by $\Delta\theta(\text{VPD}|\text{SM})$ and $\Delta\theta(\text{SM}|\text{VPD})$, calculated from
 327 the top 20% versus bottom 20% contrasts within each bin and then averaged across bins. Circles
 328 denote climatic zones, while squares denote the national total. θ was Z-score standardized in this
 329 analysis.
 330

331 Pooled binning analysis showed that θ varied nonlinearly along the joint SM–VPD gradient in
 332 both forest types, with relatively high values occurring under intermediate SM and moderate-to-
 333 high VPD conditions, and lower values toward both the wet/low-VPD and dry/high-VPD ends of

334 the gradient (Figure 4a,b). The contrast analysis further revealed clear differences in the relative
335 effects of SM and VPD (Figure 4c). At the national scale, NF showed a much stronger SM-related
336 contrast than VPD-related contrast [$\Delta\theta(\text{SM}|\text{VPD}) = -0.396$ versus $\Delta\theta(\text{VPD}|\text{SM}) = -0.065$], whereas
337 PF showed the opposite pattern, with a much stronger VPD-related contrast [$\Delta\theta(\text{VPD}|\text{SM}) = 0.228$
338 versus $\Delta\theta(\text{SM}|\text{VPD}) = 0.009$]. Across climatic zones, NF exhibited stronger VPD-related contrasts
339 in the humid and semi-arid zones but stronger SM-related contrasts in the semi-humid zone. In
340 contrast, PF was mainly VPD-dominated in the humid and semi-arid zones, while both contrasts
341 were relatively weak in the semi-humid zone. Within the pooled spatial-binning framework, these
342 results indicate that the relative roles of soil water supply and atmospheric demand differed
343 markedly between NF and PF. Zone-specific pooled SM–VPD binning patterns for NF and PF are
344 shown in Figures S14 and S15, respectively.

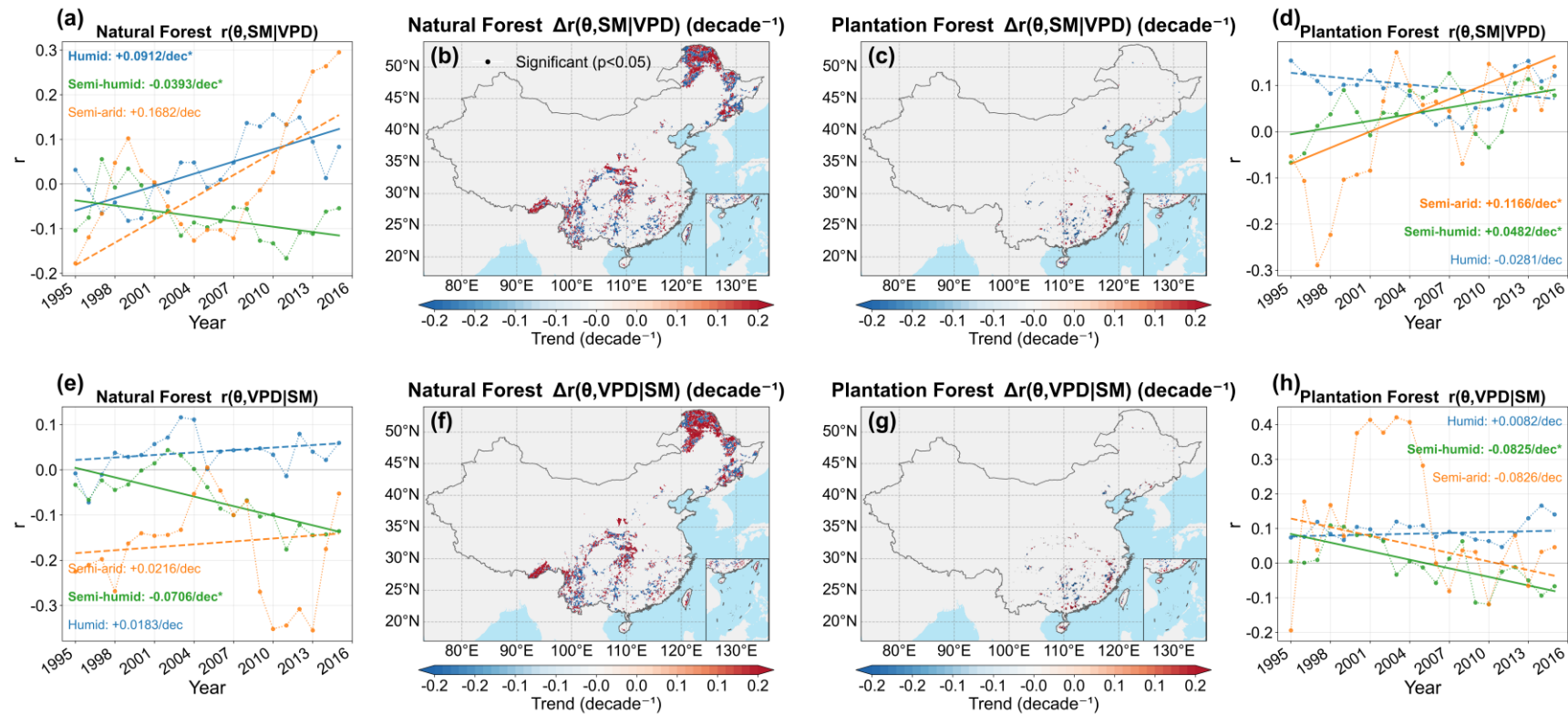
345 **3.2.2. Dynamic evolution of the independent effects of SM and VPD**

346 Partial-correlation analysis revealed that the independent associations of θ with both SM and
347 VPD were predominantly negative and were generally stronger in PF than in NF (Figure 5). At the
348 national scale, the mean values of $r(\theta, \text{SM}|\text{VPD})$ and $r(\theta, \text{VPD}|\text{SM})$ were -0.0725 and -0.0992 in
349 NF, compared with -0.1517 and -0.1630 in PF, respectively, indicating slightly stronger VPD-
350 related associations in both forest types and overall stronger hydroclimatic constraints in PF. Across
351 climatic zones, the strongest negative partial correlations in NF occurred in the semi-arid zone,
352 especially for VPD, whereas PF showed consistently negative correlations across all zones. The
353 temporal analyses further revealed spatially heterogeneous changes in these relationships (Figure
354 6). In NF, the SM-related partial correlation became less negative in the humid and semi-arid zones,
355 while the VPD-related partial correlation also became less negative in the semi-humid zone. In PF,
356 the SM-related partial correlation became more negative in the semi-humid and semi-arid zones,
357 whereas the VPD-related partial correlation became less negative in the semi-humid zone. Overall,
358 both SM and VPD constrained θ , but the constraints were generally stronger in PF, and their
359 temporal changes were regionally differentiated rather than spatially uniform.



360

361 **Figure 5. Spatial distribution and zonal means of partial correlations between forest LAI-TF**
 362 **sensitivity (θ) and hydroclimatic factors during the growing season from 1995 to 2015. (a) and**
 363 **(b) show the spatial patterns of $r(\theta, SM|VPD)$ for natural forests (NF) and plantation forests (PF),**
 364 **respectively; (c) and (d) show the corresponding patterns of $r(\theta, VPD|SM)$. (e) and (f) show the**
 365 **mean partial correlations across climatic zones. All variables were Z-score standardized before**
 366 **analysis, and pixels with fewer than 10 years of valid data were excluded.**



367

368

Figure 6. Temporal evolution and spatial trends of partial correlations between forest LAI–TF sensitivity (θ) and hydroclimatic factors during the growing

369

season from 1995 to 2015. (a) and (d) show the temporal evolution of zone-averaged $r(\theta, SM | VPD)$ for NF and PF, respectively; (b) and (c) show the corresponding

370

spatial trends. (e) and (h) show the temporal evolution of zone-averaged $r(\theta, VPD | SM)$ for NF and PF, respectively; (f) and (g) show the corresponding spatial

371

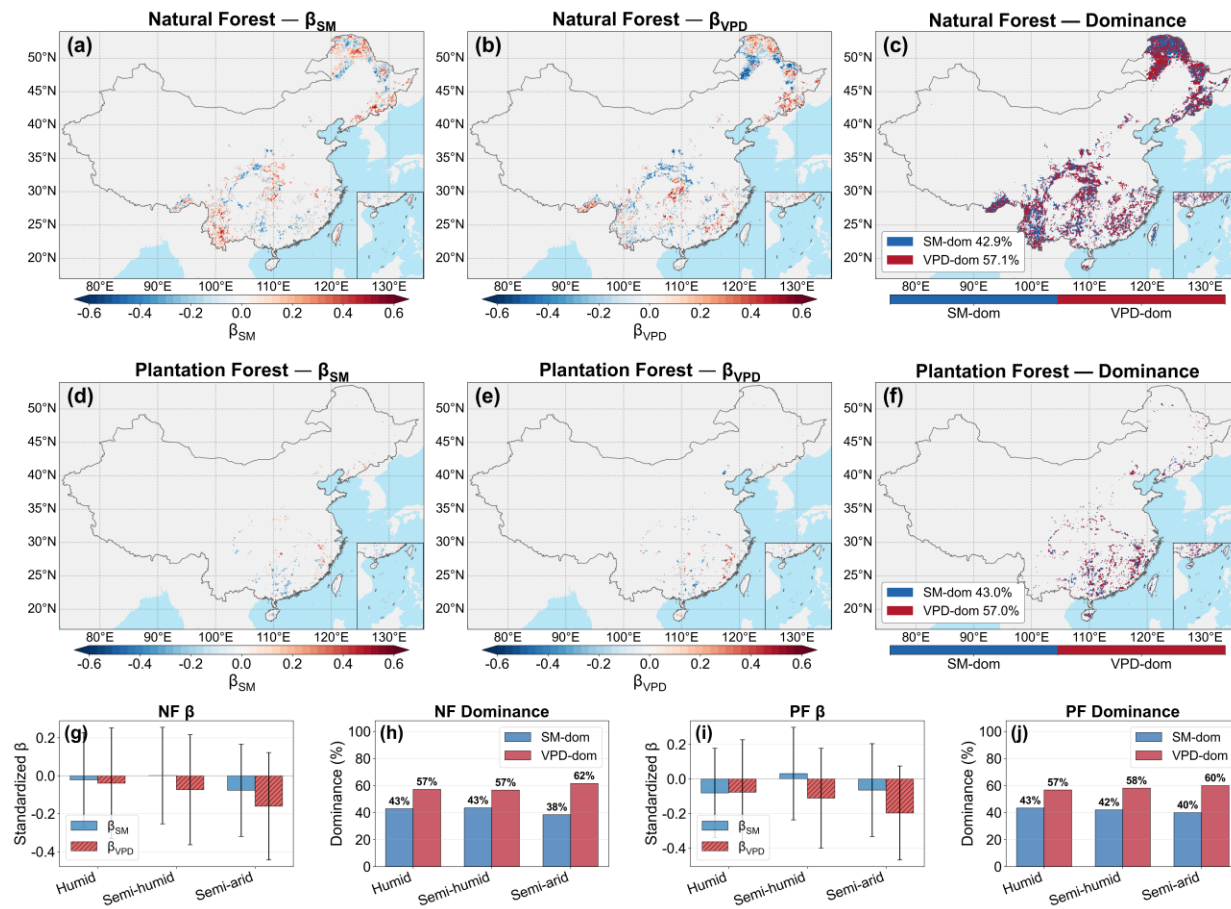
trends. Trend slopes were estimated using the Theil–Sen estimator, and significant pixels according to the variance-corrected Mann–Kendall test ($p < 0.05$) are indicated

372

by black dots.

373 **3.2.3. Quantification and spatiotemporal heterogeneity of dominant**
374 **hydrological drivers**

375 Ridge regression showed that both SM and VPD were generally negatively associated with θ ,
376 but the magnitude was usually stronger for VPD (Figure 7). At the national scale, both NF and PF
377 remained slightly more VPD-dominated in terms of the present spatial pattern, with mean relative
378 contributions of VPD of 0.541 and 0.534 in NF and PF, respectively. Consistently, VPD-dominated
379 pixels accounted for 57.1% of all NF pixels and 57.0% of all PF pixels, compared with 42.9% and
380 43.0%, respectively, for SM-dominated pixels. The relative-contribution and dominance statistics
381 therefore consistently indicated a modest present-day advantage of VPD over SM, particularly in
382 the semi-arid zone. The trend analysis further indicated a general strengthening of the SM effect
383 and a weakening of the VPD effect in several regions, especially across semi-humid to semi-arid
384 areas (Figure 8). Within the pixel-wise temporal analysis, these results suggest that VPD explained
385 a slightly larger share of the spatial pattern of θ , whereas the relative role of SM increased over time.
386 RC and VIF supported the robustness of this interpretation (Figure S16).



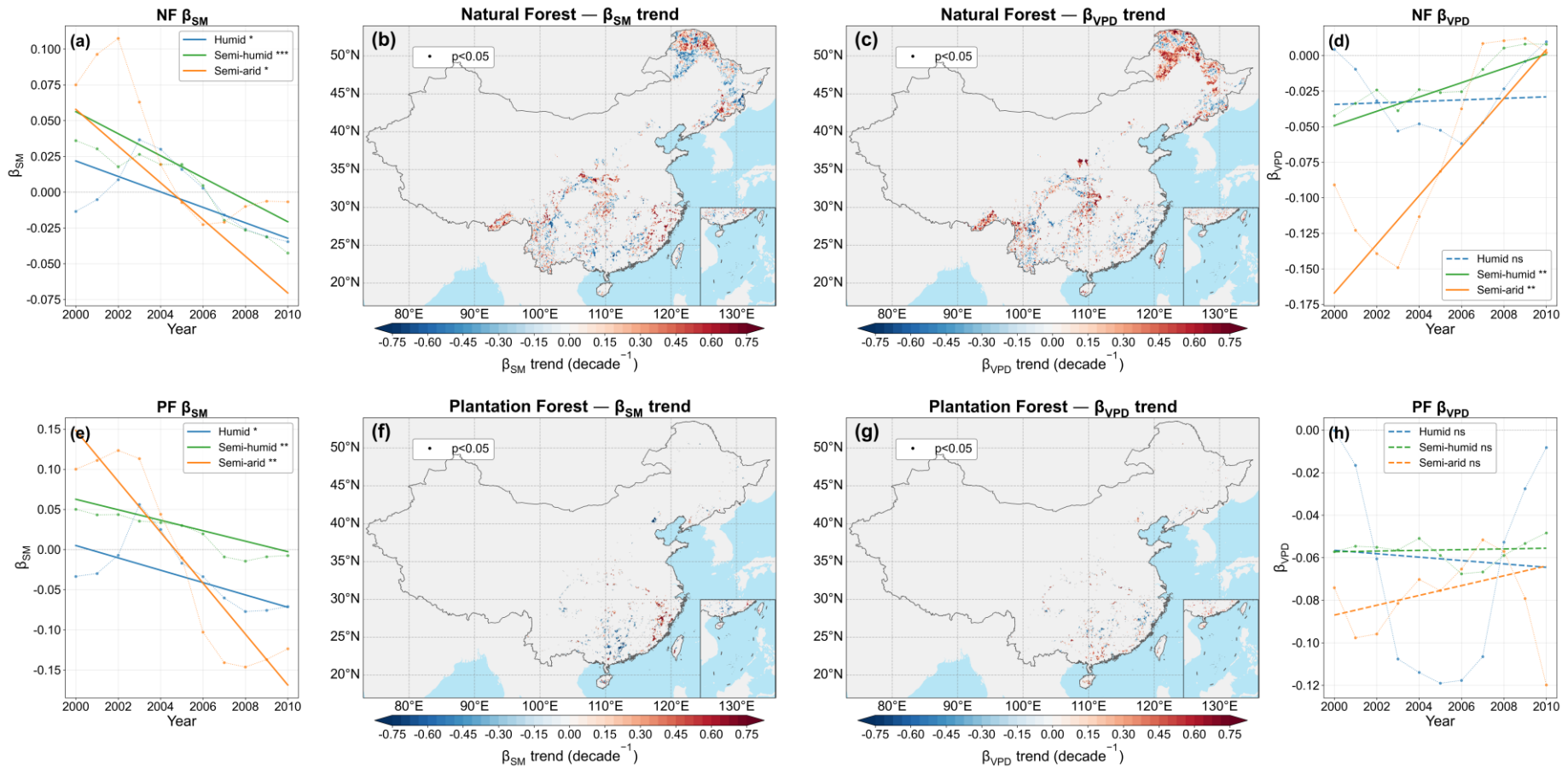
387

388 **Figure 7. Spatial distribution of ridge-regression standardized coefficients and dominant hydrological driver for forest θ .** For natural forests (NF), (a) and (b)

389 show the spatial distributions of β_{SM} and β_{VPD} , respectively, and (c) shows the corresponding dominance pattern. (d)–(f) show the same results for plantation forests

390 (PF). (g) and (i) summarize the zonal means and variability of β_{SM} and β_{VPD} for NF and PF, respectively, and (h) and (j) show the fractions of SM- and VPD-dominated

391 pixels across climatic zones. Warm colors indicate positive coefficients and cool colors indicate negative coefficients; blue and red in dominance maps denote SM-
 392 dominated and VPD-dominated pixels, respectively.

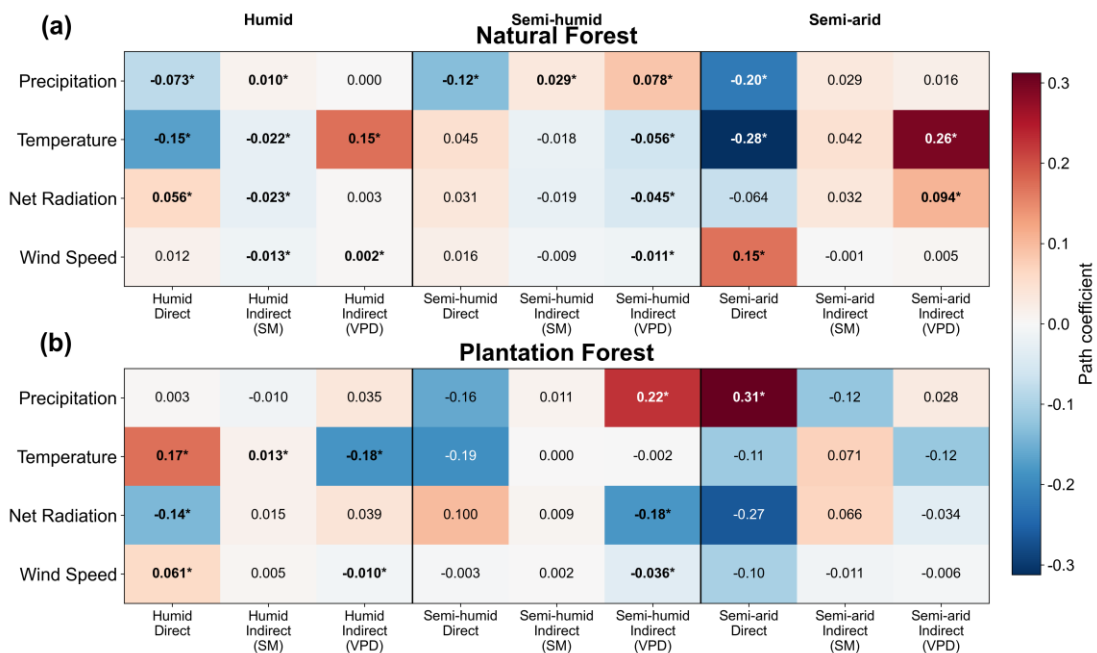


393
 394 **Figure 8. Temporal evolution and spatial trends of ridge-regression coefficients for forest θ** (a) and (e) show the temporal evolution of zone-averaged β_{SM} for NF

395 and PF, respectively; (b) and (f) show the corresponding spatial trends in β_{SM} . (d) and (h) show the temporal evolution of zone-averaged β_{VPD} for NF and PF, respectively;
396 (c) and (g) show the corresponding spatial trends in β_{VPD} . Trend slopes were estimated using the Theil–Sen estimator, and significant pixels based on the Mann–Kendall
397 test ($p < 0.05$) are indicated by black dots. Solid trend lines indicate significant trends, and dashed lines indicate non-significant trends.

398 **3.3. Pathway attribution of macro-climate effects on θ**

399 Pathway analysis indicated that the effects of macroclimate change on θ varied strongly among
 400 drivers, climatic zones, and forest types (Figure 9). In natural forests (NF), precipitation generally
 401 showed negative direct effects, especially in the semi-humid and semi-arid zones, while its indirect
 402 effects differed among pathways, including positive VPD-mediated effects in humid and semi-arid
 403 zones. Temperature was the most consistent negative direct driver in NF, with particularly strong
 404 negative effects in humid and semi-arid regions, while its indirect effects differed according to
 405 pathway, including positive VPD-mediated effects in humid and semi-arid zones. In plantation
 406 forests (PF), the pathway structure was more heterogeneous; specifically, precipitation showed a
 407 significant positive direct effect in the semi-arid zone, temperature showed opposite indirect effects
 408 through SM and VPD in the humid zone, and net radiation and wind speed mainly exerted pathway-
 409 specific effects in humid and semi-humid regions. Overall, the pathway coefficients indicated strong
 410 dependence on hydroclimatic context and forest type in how macroclimate trends were associated
 411 with changes in θ , with no single pathway dominating across all climate drivers and zones. A
 412 supplementary mediator-specification comparison showed that the direction of VPD-mediated
 413 indirect effects was generally more robust across single-mediator and joint models than that of SM-
 414 mediated effects, whereas SM-mediated pathways were more sensitive to model specification under
 415 SM–VPD coupling (Figure S19).



416

417 **Figure 9. Heatmap of pathway coefficients across climate zones for natural and plantation**
418 **forests.** Standardized path coefficients show the decomposition of the effects of four macroclimate
419 drivers (precipitation, temperature, net radiation, and wind speed) on θ_{total} trends into direct
420 effects and indirect effects mediated by SM and VPD for natural forests (a) and plantation forests
421 (b). Rows correspond to the four macro-climate drivers, while columns are grouped by climate zone
422 (humid, semi-humid, and semi-arid), each subdivided into direct effects, indirect effects via SM,
423 and indirect effects via VPD. Cell values are standardized coefficients from parallel dual-mediation
424 pathway analysis, and asterisks indicate significance at the 95% level (i.e., bootstrap confidence
425 interval excludes zero). Warm colors indicate positive effects, while cool colors indicate negative
426 effects.

427 **4. Discussion**

428 **4.1. Nonlinear hydroclimatic regulation of θ**

429 The joint SM–VPD analysis shows that θ was highest under intermediate SM and moderate-
430 to-high VPD, corresponding to relatively strong atmospheric demand, and declined toward both
431 wetter/low-demand and drier/high-demand conditions (Figure 4; Figures S14–S15). This pattern
432 indicates that increased leaf area enhances TF most effectively when water supply is sufficient but
433 not excessive and evaporative demand is strong enough to sustain canopy transpiration. Once soil
434 water becomes limiting or atmospheric demand becomes too strong, stomatal regulation
435 increasingly constrains transpiration to avoid hydraulic damage, so the marginal gain in
436 transpiration per unit increase in LAI declines (Novick et al., 2016; Grossiord et al., 2020;
437 McDowell et al., 2022). Under wetter and weak-demand conditions, the capacity of additional leaf
438 area to increase TF is also reduced because energy limitations, weaker canopy–atmosphere coupling,
439 and larger non-transpirational evaporation fractions all weaken the translation of additional leaf area
440 into transpiration (Konings et al., 2017; Stoy et al., 2019). The supplementary θ diagnostics further
441 suggest that this nonlinearity cannot be explained solely as a bounded geometric effect of TF; part
442 of the long-term change also reflects shifts in the LAI–TF relationship itself (Figures S6–S13).

443 **4.2. Long-term weakening of the LAI enhancement effect on TF**

444 The widespread decline in θ , especially across semi-humid to semi-arid transition zones,
445 indicates that the capacity of increasing LAI to enhance TF has weakened over the last three decades

446 (Figure 3). This trend is consistent with a background of warming, rising VPD, and increasing
447 frequency of soil moisture limitation, all of which reduce the effective transpiration response of
448 forests to additional canopy development (Yuan et al., 2019; Lian et al., 2020; Denissen et al., 2022).
449 Rising atmospheric CO₂ may also have contributed to this decline by lowering stomatal conductance
450 and increasing intrinsic water-use efficiency, thereby reducing transpiration demand per unit leaf
451 area even where greening continued (Keenan et al., 2013; Keenan et al., 2016; Lavergne et al., 2019;
452 Liang et al., 2023). At the same time, the supplementary analyses are more consistent with
453 interpreting CO₂ as a temporally coherent background forcing rather than a spatially heterogeneous
454 driver of θ across China's forests (Figure S17; Table S1). Stand development may likewise have
455 modulated this trajectory. Age-related changes in stand structure, rooting depth, canopy roughness,
456 and interception can shift the partitioning of evapotranspiration between transpiration and non-
457 transpirational components, and therefore alter the LAI–TF relationship even without large changes
458 in total leaf area (Fan et al., 2017; Forrester, 2015). However, the age-stratified results show that the
459 higher θ in NF than in PF persisted across age groups, and including stand age did not overturn the
460 broad interpretation of the relative roles of SM and VPD, although the magnitude of change was
461 heterogeneous across forest types and climatic zones (Figure S18; Table S2). Together, these results
462 suggest that CO₂ rise and stand development may act as background modifiers of θ , while the
463 dominant large-scale patterns remain primarily associated with hydroclimatic variability.

464 **4.3. Temporal changes in hydroclimatic effects on θ**

465 Partial correlation, ridge regression, and pathway analysis consistently indicate that the
466 hydroclimatic controls on θ have changed over time, with the relative role of SM strengthening and
467 that of VPD weakening in many regions (Figures 5–9). This does not mean that atmospheric demand
468 has ceased to matter; VPD still explains a slightly larger share of the present spatial pattern of θ , as
469 also supported by the dominance statistics and multicollinearity diagnostics (Figure 7; Figure S16).
470 The more important point is that the sensitivity of θ to soil moisture limitation has intensified under
471 recent climatic conditions. This interpretation is physically consistent with the increasing prevalence
472 of water-limited ecosystem behavior under warming, in which rising evaporative demand is
473 increasingly translated into ecological stress through soil-water depletion rather than through
474 atmospheric forcing alone (Berg et al., 2016; Denissen et al., 2022). Once ecosystems approach

475 critical soil-moisture thresholds more frequently, stomatal and hydraulic regulation become more
476 tightly constrained by water supply, and the explanatory role of SM rises accordingly (Fu et al.,
477 2022; Liu et al., 2025). The pathway results add the same message at a broader scale: temperature
478 exerted generally negative effects on θ , whereas the effects of precipitation and radiation varied by
479 forest type and climatic zone, implying that macroclimate trends influence θ through multiple
480 hydroclimatic pathways rather than through a single dominant mechanism.

481 **4.4. Contrasting ecohydrological responses of natural and plantation forests**

482 The contrast between natural and plantation forests remained one of the clearest features of the
483 analysis. NF consistently showed higher θ , and high- θ values in NF were maintained across a wider
484 range of SM–VPD backgrounds, whereas PF showed lower θ and a more restricted range of
485 hydroclimatic conditions under which high θ occurred. This pattern likely reflects differences
486 between long-term spatial hydroclimatic contrasts and within-pixel temporal variability. Spatial
487 contrasts integrate longer-term differences in stand structure, species composition, hydraulic
488 diversity, and belowground water access, whereas temporal anomalies are expressed more directly
489 through canopy–atmosphere coupling and stomatal–hydraulic regulation during drought (Martínez-
490 Vilalta & García-Forner, 2017; Grossiord et al., 2020; Novick et al., 2024; Bachofen et al., 2024).
491 Under this interpretation, the broader hydroclimatic response of NF may reflect the greater structural
492 and functional heterogeneity often associated with natural forests, while the narrower response of
493 PF may reflect the relative structural simplification typical of many plantation stands. This
494 interpretation is also consistent with evidence that higher hydraulic diversity can buffer ecosystem
495 drought responses (Anderegg et al., 2018). The age-stratified supplementary results are consistent
496 with this interpretation, because the higher θ in NF than in PF persisted across age classes and this
497 pattern is therefore unlikely to be explained solely by stand age.

498 **4.5. Implications and limitations**

499 These results imply that further greening will not necessarily translate into proportionally
500 higher transpiration fractions under continued warming and drying. In regions where hydroclimatic
501 water stress is increasing, especially across semi-humid to semi-arid transition zones, the
502 ecohydrological consequences of increasing canopy leaf area depend increasingly on soil water

503 supply, and this dependence appears more evident in plantation forests than in natural forests. This
504 has direct management implications: plantation design may benefit from greater rooting-depth and
505 trait diversity and from stand structures that reduce rapid soil-water depletion, whereas natural
506 forests may benefit more from maintaining multilayer canopy structure and hydraulic diversity
507 under rising atmospheric demand. Several limitations should remain explicit. A nationwide in situ
508 benchmark for θ trends is not yet available because long-term observations that simultaneously
509 resolve transpiration partitioning, LAI dynamics, and stand development remain too sparse across
510 China's forests. We therefore evaluated robustness through cross-product consistency rather than
511 direct site-based validation. In addition, because θ , SM, and VPD were analyzed from growing-
512 season aggregates and moving-window series, the results characterize seasonal-to-interannual
513 hydroclimatic controls rather than instantaneous stomatal responses to short-lived atmospheric
514 fluctuations. Even with these constraints, the convergence among the main analyses, the
515 supplementary robustness checks, and the CO₂- and age-sensitivity diagnostics supports the central
516 inference that the enhancement of TF by increasing LAI has weakened across China's forests and
517 is increasingly shaped by soil moisture limitation.

518 **5. Conclusion**

519 Across China's forests, the enhancement of TF caused by increased LAI has weakened during
520 1990–2020. VPD still explains a slightly larger share of the present spatial pattern of θ , but the role
521 of SM has strengthened over this timespan, indicating there has been an increase in SM limitation.
522 Differences between NF and PF were obvious: NF maintained higher θ values, whereas PF showed
523 a greater long-term decline in θ . Collectively, these results indicate that continued greening under
524 warming will not necessarily result in proportionally higher TF, particularly in semi-humid to semi-
525 arid transition regions.

526 **Author contributions**

527 Xiao Zhang performed the analysis, prepared the figures, and drafted the manuscript. Xinxiao
528 Yu contributed to the study design, interpretation of the results, and manuscript revision. Guodong
529 Jia conceived and supervised the study, contributed to the analytical framework, and revised the
530 manuscript. All authors discussed the results and approved the final manuscript.

531 **Competing interests**

532 The authors declare that they have no conflict of interest.

533 **Code and data availability**

534 The datasets used in this study are publicly available from the sources cited in Table 1. The
535 processed data and code supporting the findings of this study are available from the corresponding
536 author upon reasonable request.

537 **Funding**

538 This research was supported by the National Natural Science Foundation of China (grant
539 numbers 42277062, 41977149, and 42230714).

540

541 **References**

- 542 Anderegg, W.R.L., Konings, A.G., Trugman, A.T., Yu, K., Bowling, D.R., Gabbitas, R., Karp,
543 D.S., Pacala, S., Sperry, J.S., Sulman, B.N. and Zenes, N. (2018) Hydraulic diversity of forests
544 regulates ecosystem resilience during drought. *Nature*, 561, 538–541. doi:10.1038/s41586-018-
545 0539-7
- 546 Bachofen, C., Tumber-Dávila, S.J., Mackay, D.S., McDowell, N.G., Carminati, A., Klein, T.,
547 Stocker, B.D., Mencuccini, M. and Grossiord, C. (2024) Tree water uptake patterns across the globe.
548 *New Phytologist*, 242, 1891–1910. doi:10.1111/nph.19762
- 549 Berg, A., Findell, K., Lintner, B., Giannini, A., Seneviratne, S.I., van den Hurk, B., Lorenz, R.,
550 Pitman, A.J., Hagemann, S., Meier, A., Cheruy, F., Ducharne, A., Malyshev, S. and Milly, P.C.D.
551 (2016) Land–atmosphere feedbacks amplify aridity increase over land under global warming.
552 *Nature Climate Change*, 6, 869–874. doi:10.1038/nclimate3029
- 553 Buck, A.L. (1981) New equations for computing vapor pressure and enhancement factor.
554 *Journal of Applied Meteorology*, 20, 1527–1532. doi:10.1175/1520-
555 0450(1981)020<1527:NEFCVP>2.0.CO;2
- 556 Chen, H., Wei, Y. and Huang, J.J. (2024) Widespread increase in plant transpiration driven by
557 global greening. *Global and Planetary Change*, 235, 104395. doi:10.1016/j.gloplacha.2024.104395
- 558 Chen, H., Zhu, G., Shang, S., Qin, W., Zhang, Y., Su, Y., Zhang, K., Zhu, Y. and Xu, C. (2022)
559 Uncertainties in partitioning evapotranspiration by two remote sensing-based models. *Journal of*
560 *Hydrology*, 604, 127223. doi:10.1016/j.jhydrol.2021.127223
- 561 Cheng, K., Chen, Y., Xiang, T., Yang, H., Liu, W., Ren, Y., Guan, H., Hu, T., Ma, Q. and Guo,
562 Q. (2024a) A 2020 forest age map for China with 30 m resolution. *Earth System Science Data*, 16,
563 803–819. doi:10.5194/essd-16-803-2024.
- 564 Cheng, K., Yang, H., Guan, H., Ren, Y., Chen, Y., Chen, M., Yang, Z., Lin, D., Liu, W., Xu,
565 J., Xu, G., Ma, K. and Guo, Q. (2024b) Unveiling China’s natural and planted forest spatial–
566 temporal dynamics from 1990 to 2020. *ISPRS Journal of Photogrammetry and Remote Sensing*,
567 209, 37–50. doi:10.1016/j.isprsjprs.2024.01.024
- 568 Cheng, K., Zhang, Y., Yang, H., Ren, Y., Xiang, T., Chen, Y., Yang, Z., Chen, M., Xu, J.,
569 Huang, G., Xu, G., Tao, S., Yu, Z. and Guo, Q. (2025) China’s naturally regenerated forests
570 currently have greater aboveground carbon accumulation rates than newly planted forests.
571 *Communications Earth & Environment*, 6, 345. doi:10.1038/s43247-025-02323-z
- 572 Denissen, J.M.C., Teuling, A.J., Pitman, A.J., Koirala, S., Migliavacca, M., Li, W., Reichstein,
573 M., Winkler, A.J., Zhan, C. and Orth, R. (2022) Widespread shift from ecosystem energy to water
574 limitation with climate change. *Nature Climate Change*, 12, 677–684. doi:10.1038/s41558-022-
575 01403-8
- 576 Fan, Y., Miguez-Macho, G., Jobbágy, E.G., Jackson, R.B. and Otero-Casal, C. (2017)
577 Hydrologic regulation of plant rooting depth. *Proceedings of the National Academy of Sciences of*
578 *the United States of America*, 114, 10572–10577. doi:10.1073/pnas.1712381114
- 579 Farley, K.A., Jobbágy, E.G. and Jackson, R.B. (2005) Effects of afforestation on water yield:
580 a global synthesis with implications for policy. *Global Change Biology*, 11, 1565–1576.
581 doi:10.1111/j.1365-2486.2005.01011.x
- 582 Farooq, T.H., Shakoor, A., Wu, X., Li, Y., Rashid, M.H.U., Zhang, X., Gilani, M.M., Kumar,
583 U., Chen, X. and Yan, W. (2021) Perspectives of plantation forests in the sustainable forest

584 development of China. *iForest - Biogeosciences and Forestry*, 14, 166–174. doi:10.3832/ifor3551-
585 014.

586 Forrester, D.I. (2015) Transpiration and water-use efficiency in mixed-species forests versus
587 monocultures: effects of tree size, stand density and season. *Tree Physiology*, 35, 289–304.
588 doi:10.1093/treephys/tpv011

589 Fu, Z., Ciais, P., Feldman, A., Gentine, P., Makowski, D., Prentice, I.C., Stoy, P.C., Bastos, A.
590 and Wigneron, J.-P. (2022) Critical soil moisture thresholds of plant water stress in terrestrial
591 ecosystems. *Science Advances*, 8, eabq7827. doi:10.1126/sciadv.abq7827

592 Grossiord, C., Buckley, T.N., Cernusak, L.A., Novick, K.A., Poulter, B., Siegwolf, R.T.W.,
593 Sperry, J.S. and McDowell, N.G. (2020) Plant responses to rising vapor pressure deficit. *New*
594 *Phytologist*, 226, 1550–1566. doi:10.1111/nph.16485

595 Hirschi, M., Stradiotti, P., Crezee, B., Dorigo, W. and Seneviratne, S.I. (2025) Potential of
596 long-term satellite observations and reanalysis products for characterising soil drying: trends and
597 drought events. *Hydrology and Earth System Sciences*, 29, 397–425. doi:10.5194/hess-29-397-2025

598 Hu, Y., Wei, F., Fu, B. and Zhang, W. (2023) Ecosystems in China have become more sensitive
599 to changes in water demand since 2001. *Communications Earth & Environment*, 4, 444.
600 doi:10.1038/s43247-023-01105-9

601 Huang, X., Liang, S., Ziegler, A.D. and Zeng, Z. (2025) Decoupling vegetation and soil-
602 moisture interaction in evapotranspiration interannual variability. *iScience*, 28, 113008.
603 doi:10.1016/j.isci.2025.113008

604 Intergovernmental Panel on Climate Change (IPCC) (2023) Weather and climate extreme
605 events in a changing climate. In: *Climate Change 2021 – The Physical Science Basis: Working*
606 *Group I Contribution to the Sixth Assessment Report of the Intergovernmental Panel on Climate*
607 *Change*. Cambridge University Press, Cambridge, pp. 1513–1766.
608 doi:10.1017/9781009157896.013

609 Jin, Z., You, Q., Zuo, Z., Li, M., Sun, G., Pepin, N. and Wang, L. (2023) Weakening
610 amplification of grassland greening to transpiration fraction of evapotranspiration over the Tibetan
611 Plateau during 2001–2020. *Agricultural and Forest Meteorology*, 341, 109661.
612 doi:10.1016/j.agrformet.2023.109661

613 Keenan, T.F., Hollinger, D.Y., Bohrer, G., Dragoni, D., Munger, J.W., Schmid, H.P. and
614 Richardson, A.D. (2013) Increase in forest water-use efficiency as atmospheric carbon dioxide
615 concentrations rise. *Nature*, 499, 324–327. doi:10.1038/nature12291

616 Keenan, T.F., Prentice, I.C., Canadell, J.G., Williams, C.A., Wang, H., Raupach, M. and
617 Collatz, G.J. (2016) Recent pause in the growth rate of atmospheric CO₂ due to enhanced terrestrial
618 carbon uptake. *Nature Communications*, 7, 13428. doi:10.1038/ncomms13428

619 Koehler, T., Wankmüller, F.J.P., Sadok, W. and Carminati, A. (2023) Transpiration response
620 to soil drying versus increasing vapor pressure deficit in crops: physical and physiological

621 mechanisms and key plant traits. *Journal of Experimental Botany*, 74, 4789–4807.
622 doi:10.1093/jxb/erad235

623 Konings, A.G., Williams, A.P. and Gentine, P. (2017) Sensitivity of grassland productivity to
624 aridity controlled by stomatal and xylem regulation. *Nature Geoscience*, 10, 284–288.
625 doi:10.1038/ngeo2903

626 Lavergne, A., Graven, H., De Kauwe, M.G., Keenan, T.F., Medlyn, B.E. and Prentice, I.C.
627 (2019) Observed and modelled historical trends in the water-use efficiency of plants and ecosystems.
628 *Global Change Biology*, 25, 2242–2257. doi:10.1111/gcb.14634

629 Li, C., Han, J., Liu, Z., Tu, Z. and Yang, H. (2024) A harmonized global gridded transpiration
630 product based on collocation analysis. *Scientific Data*, 11, 604. doi:10.1038/s41597-024-03425-7

631 Lian, X., Piao, S., Li, L.Z.X., Li, Y., Huntingford, C., Ciais, P., Cescatti, A., Janssens, I.A.,
632 Peñuelas, J., Buermann, W., Chen, A., Li, X., Myneni, R.B., Wang, X., Wang, Y., Yang, Y., Zeng,
633 Z., Zhang, Y. and McVicar, T.R. (2020) Summer soil drying exacerbated by earlier spring greening
634 of northern vegetation. *Science Advances*, 6, eaax0255. doi:10.1126/sciadv.aax0255

635 Liang, X., Wang, D., Ye, Q., Zhang, J., Liu, M., Liu, H., Yu, K., Wang, Y., Hou, E., Zhong,
636 B., Xu, L., Lv, T., Peng, S., Lu, H., Sicard, P., Anav, A. and Ellsworth, D.S. (2023) Stomatal
637 responses of terrestrial plants to global change. *Nature Communications*, 14, 2188.
638 doi:10.1038/s41467-023-37934-7

639 Liu, L., Gudmundsson, L., Hauser, M., Qin, D., Li, S. and Seneviratne, S.I. (2020) Soil
640 moisture dominates dryness stress on ecosystem production globally. *Nature Communications*, 11,
641 4892. doi:10.1038/s41467-020-18631-1

642 Liu, Y., Kumar, M., Katul, G.G., Feng, X. and Konings, A.G. (2020) Plant hydraulics
643 accentuates the effect of atmospheric moisture stress on transpiration. *Nature Climate Change*, 10,
644 691–695. doi:10.1038/s41558-020-0781-5

645 Liu, Y., Lin, Z., Wang, Z., Chen, X., Han, P., Wang, B., Wang, Z., Wen, Z., Shi, H., Zhang, Z.
646 and Zhang, W. (2023) Discriminating the impacts of vegetation greening and climate change on the
647 changes in evapotranspiration and transpiration fraction over the Yellow River Basin. *Science of the*
648 *Total Environment*, 904, 166926. doi:10.1016/j.scitotenv.2023.166926

649 Liu, Y., Wang, Y., Zhao, Y., Chen, S., Wang, L., Yang, W., Li, X., Li, X., Lei, H., Chang, H.
650 and others (2025) Evapotranspiration stress intensifies with enhanced sensitivity to soil moisture
651 deficits in a rapidly greening China. *Hydrology and Earth System Sciences*, 29, 3379–3404.
652 doi:10.5194/hess-29-3379-2025

653 Lu, W.W., Yu, X.X., Jia, G., Li, H. and Liu, Z. (2018) Responses of intrinsic water-use
654 efficiency and tree growth to climate change in semi-arid areas of North China. *Scientific Reports*,
655 8, 308. doi:10.1038/s41598-017-18694-z

656 Martínez-Vilalta, J. and Garcia-Forner, N. (2017) Water potential regulation, stomatal
657 behaviour and hydraulic transport under drought: deconstructing the iso/anisohydric concept. *Plant,*
658 *Cell & Environment*, 40, 962–976. doi:10.1111/pce.12846

659 McDowell, N.G., Sapes, G., Pivovarov, A., Adams, H.D., Allen, C.D., Anderegg, W.R.L.,
660 Arend, M., Breshears, D.D., Brodrick, T., Choat, B., Cochard, H., De Cáceres, M., De Kauwe, M.G.,
661 Grossiord, C., Hammond, W.M., Hartmann, H., Hoch, G., Kahmen, A., Klein, T., Mackay, D.S.,
662 Mantova, M., Martínez-Vilalta, J., Medlyn, B.E., Mencuccini, M., Nardini, A., Oliveira, R.S., Sala,
663 A., Tissue, D.T., Torres-Ruiz, J.M., Trowbridge, A.M., Trugman, A.T., Wiley, E. and Xu, C. (2022)

664 Mechanisms of woody-plant mortality under rising drought, CO₂ and vapour pressure deficit.
665 *Nature Reviews Earth & Environment*, 3, 294–308. doi:10.1038/s43017-022-00272-1

666 Niu, Z., He, H., Zhu, G., Ren, X., Zhang, L. and Zhang, K. (2020) A spatial-temporal
667 continuous dataset of the transpiration to evapotranspiration ratio in China from 1981–2015.
668 *Scientific Data*, 7, 369. doi:10.1038/s41597-020-00693-x

669 Novick, K.A., Ficklin, D.L., Grossiord, C., Konings, A.G., Martínez-Vilalta, J., Sadok, W.,
670 Trugman, A.T., Williams, A.P., Wright, A.J., Abatzoglou, J.T., Dannenberg, M.P., Gentine, P.,
671 Guan, K., Johnston, M.R., Lowman, L.E.L., Moore, D.J.P. and McDowell, N.G. (2024) The impacts
672 of rising vapour pressure deficit in natural and managed ecosystems. *Plant, Cell & Environment*,
673 47, 3561–3589. doi:10.1111/pce.14846

674 Novick, K.A., Ficklin, D.L., Stoy, P.C., Williams, C.A., Bohrer, G., Oishi, A.C., Papuga, S.A.,
675 Blanken, P.D., Noormets, A., Sulman, B.N., Scott, R.L., Wang, L. and Phillips, R.P. (2016) The
676 increasing importance of atmospheric demand for ecosystem water and carbon fluxes. *Nature*
677 *Climate Change*, 6, 1023–1027. doi:10.1038/nclimate3114

678 Qing, Y., Wang, S., Ancell, B.C. and Yang, Z.-L. (2022) Accelerating flash droughts induced
679 by the joint influence of soil moisture depletion and atmospheric aridity. *Nature Communications*,
680 13, 1139. doi:10.1038/s41467-022-28752-4

681 Schlesinger, W.H. and Jasechko, S. (2014) Transpiration in the global water cycle. *Agricultural*
682 *and Forest Meteorology*, 189–190, 115–117. doi:10.1016/j.agrformet.2014.01.011

683 Song, J., Zhou, S., Yu, B., Li, Y., Liu, Y., Yao, Y., Wang, S. and Fu, B. (2024) Serious
684 underestimation of reduced carbon uptake due to vegetation compound droughts. *npj Climate and*
685 *Atmospheric Science*, 7, 23. doi:10.1038/s41612-024-00571-y

686 Sperry, J.S., Venturas, M.D., Anderegg, W.R.L., Mencuccini, M., Mackay, D.S., Wang, Y.
687 and Love, D.M. (2017) Predicting stomatal responses to the environment from the optimization of
688 photosynthetic gain and hydraulic cost. *Plant, Cell & Environment*, 40, 816–830.
689 doi:10.1111/pce.12852

690 Stoy, P.C., El-Madany, T.S., Fisher, J.B., Gentine, P., Gerken, T., Good, S.P., Klosterhalfen,
691 A., Liu, S., Miralles, D.G., Perez-Priego, O., Rigden, A.J., Skaggs, T.H., Wohlfahrt, G., Anderson,
692 R.G., Coenders-Gerrits, A.M.J., Jung, M., Maes, W.H., Mammarella, I., Mauder, M., Migliavacca,
693 M., Nelson, J.A., Poyatos, R., Reichstein, M., Scott, R.L. and Wolf, S. (2019) Reviews and
694 syntheses: turning the challenges of partitioning ecosystem evaporation and transpiration into
695 opportunities. *Biogeosciences*, 16, 3747–3775. doi:10.5194/bg-16-3747-2019

696 Sun, S., Liu, Y., Chen, H., Ju, W., Xu, C.-Y., Liu, Y., Zhou, B., Zhou, Y., Zhou, Y. and Yu,
697 M. (2022) Causes for the increases in both evapotranspiration and water yield over vegetated

698 mainland China during the last two decades. *Agricultural and Forest Meteorology*, 324, 109118.
699 doi:10.1016/j.agrformet.2022.109118

700 Wei, Z., Yoshimura, K., Wang, L., Miralles, D.G., Jasechko, S. and Lee, X. (2017) Revisiting
701 the contribution of transpiration to global terrestrial evapotranspiration. *Geophysical Research*
702 *Letters*, 44, 2792–2801. doi:10.1002/2016GL072235

703 Xu, H., Yue, C., Zhang, Y., Liu, D. and Piao, S. (2023) Forestation at the right time with the
704 right species can generate persistent carbon benefits in China. *Proceedings of the National Academy*
705 *of Sciences of the United States of America*, 120, e2304988120. doi:10.1073/pnas.2304988120

706 Xu, L., Chen, N. and Zhang, X. (2019) Global drought trends under 1.5 and 2 °C warming.
707 *International Journal of Climatology*, 39, 2375–2385. doi:10.1002/joc.5958

708 Yuan, W., Zheng, Y., Piao, S., Ciais, P., Lombardozzi, D., Wang, Y., Ryu, Y., Chen, G., Dong,
709 W., Hu, Z., Jain, A.K., Jiang, C., Kato, E., Li, S., Lienert, S., Liu, S., Nabel, J.E.M.S., Qin, Z., Quine,
710 T., Sitch, S., Smith, W.K., Wang, F., Wu, C., Xiao, Z. and Yang, S. (2019) Increased atmospheric
711 vapor pressure deficit reduces global vegetation growth. *Science Advances*, 5, eaax1396.
712 doi:10.1126/sciadv.aax1396

713 Zahra, N., Hafeez, M.B., Kausar, A., Al Zeidi, M., Asekova, S., Siddique, K.H.M. and Farooq,
714 M. (2023) Plant photosynthetic responses under drought stress: effects and management. *Journal of*
715 *Agronomy and Crop Science*, 209, 651–672. doi:10.1111/jac.12652

716 Zhang, J., Liu, N., Zhang, C., Zhang, X., He, X., Jiang, W., Li, J., Zhan, Z., Peng, D., Lv, D.
717 and Ni, S. (2025) Deep soil moisture has limited impact on mitigating drought stress effects on plant
718 transpiration in a subtropical secondary forest. *Plant and Soil*, 514, 427–444. doi:10.1007/s11104-
719 025-07398-3

720 Zhang, K., Chen, H., Ma, N., Shang, S., Wang, Y., Xu, Q. and Zhu, G. (2024) A global dataset
721 of terrestrial evapotranspiration and soil moisture dynamics from 1982 to 2020. *Scientific Data*, 11,
722 445. doi:10.1038/s41597-024-03271-7

723 Zhou, S. and Yu, B. (2025) Neglecting land–atmosphere feedbacks overestimates climate-
724 driven increases in evapotranspiration. *Nature Climate Change*, 15, 1099–1106.
725 doi:10.1038/s41558-025-02428-5

726 Zhou, S., Zhang, Y., Williams, A.P. and Gentine, P. (2019) Projected increases in intensity,
727 frequency, and terrestrial carbon costs of compound drought and aridity events. *Science Advances*,
728 5, eaau5740. doi:10.1126/sciadv.aau5740

729
730